Effects of Aerosol and Horizontal Inhomogeneity on the Broadband Albedo of Marine Stratus: Numerical Simulations

D. P. DUDA, G. L. STEPHENS, B. STEVENS, AND W. R. COTTON

Department of Atmospheric Science, Colorado State University, Fort Collins, Colorado

(Manuscript received 28 September 1995, in final form 11 June 1996)

ABSTRACT

Recent estimates of the effect of increasing amounts of anthropogenic sulfate aerosol on the radiative forcing of the atmosphere have indicated that its impact may be comparable in magnitude to the effect from increases in CO_2. Much of this impact is expected from the effects of the aerosol on cloud microphysics and the subsequent impact on cloud albedo. However, internal horizontal variations in cloud optical properties are also known to affect cloud albedo.

A solar broadband version of a 2D radiative transfer model was used to quantify the impact of enhanced aerosol concentrations and horizontal inhomogeneity on the solar broadband albedo of marine stratus. The 2D cross sections of cloud physics data taken from a set of 3D RAMS/LES simulations of marine stratus provided realistic optical property data for radiative transfer simulations. A control run using typical marine CCN concentrations and a sensitivity study using enhanced concentrations of CCN were examined.

The results of the radiative transfer calculations indicated that in unbroken marine stratus clouds the *net* horizontal transport of photons over a domain of a few kilometers was nearly zero, and the domain-average broadband albedo computed in a 2D cross section was nearly identical to the domain average calculated from a series of independent pixel approximation (IPA) calculations of the same cross section. However, the horizontal inhomogeneity does affect the cloud albedo compared to plane-parallel approximation (PPA) computations due to the nonlinear relationship between albedo and optical depth. The reduction in cloud albedo could be related to the variability of the distribution of log (cloud optical depth). These results extend the findings of Cahalan et al. to broadband solar albedos in a more realistic cloud model and suggest that accurate computation of domain-averaged broadband albedos in unbroken (or nearly unbroken) marine stratus can be made using IPA calculations with 1D radiative transfer models. Computations of the mean albedo over portions of the 3D RAMS domain show the relative increase in cloud albedo due to a 67% increase in the boundary-layer average CCN concentration was between 6% and 9%. The effects of cloud inhomogeneity on the broadband albedo as measured from the PPA bias ranged from 3% to 5%.

1. Introduction

The relationship between changes in aerosol concentrations and cloud albedo have been considered by scientists ever since Twomey (1977) hypothesized that increasing concentrations of cloud condensation nuclei (CCN) as the result of increasing levels of pollution would tend to make clouds brighter. More recently, other researchers have postulated that sources of natural CCN could also affect cloud droplet size and cloud albedo. For example, Charlson et al. (1987) have hypothesized a temperature-related CCN–albedo feedback that may partially counteract or exaggerate the effects of global warming by greenhouse gases.

Although the "Twomey effect" has been quantified by observations of ship tracks in marine stratus cloud decks (Coakley et al. 1987), the global impact of in-

creased CCN concentrations on clouds is difficult to assess. Recent climate studies have suggested that even relatively small changes in the optical properties of large-scale cloud systems may have significant effects on global climate. Slingo (1990) estimates from a global circulation model (GCM) study that decreasing the mean effective radius of low clouds across the entire planet from 10 to 8.5 μm would result in a global (cooling) radiative forcing that could offset the expected warming due to doubling the CO_2 content of the atmosphere. More recent studies by Jones et al. (1994) and Boucher and Rodhe (1994) using the parameterized effects of aerosol on clouds in a GCM show that present levels of anthropogenic aerosol produce a radiative forcing comparable to the forcing resulting from CO_2 added since 1850.

The effects of cloud microphysics on clouds have been studied considerably in the past few decades by plane-parallel radiative transfer models (RTMs), but the effects of the large-scale structure (especially horizontal inhomogeneity) of a cloud system on radiative transfer have only recently begun to be studied. Some

Corresponding author address: Dr. David P. Duda, Department of Atmospheric Science, Colorado State University, Fort Collins, CO 80523.

studies have suggested that horizontal inhomogeneity may possibly influence radiative transfer in cloud systems. Satellite observations of radiances have shown discrepancies with plane-parallel model predictions, even when the near-nadir radiances show good agreement (Stuhlmann et al. 1985; Smith et al. 1989). Using a simple cloud model, Cahalan et al. (1994a) have shown that the effects of internal horizontal inhomogeneity in an unbroken layer of marine stratus may produce a relative reduction in cloud albedo as large as 15% compared to a horizontally homogeneous cloud with the same mean optical properties. The results of Cahalan et al. (1994a) suggest that the effects of cloud structure may modify the magnitude of the Twomey CCN–albedo effect if changes in microphysics due to increased CCN concentrations lead to changes in the macrophysics (i.e., physical structure) of the cloud.

Since marine stratus cloud systems are known to have a large effect on the radiative budget of the earth–atmosphere system, it is crucial that the most important factors that influence the radiative properties of these clouds be identified. Previous estimates of the impact of CCN on cloud albedo such as those in Jones et al. (1994) are ultimately based on plane-parallel RTMs. Kim and Cess (1993) report higher values of low-level cloud albedo in near coastal boundaries compared to similar midocean clouds and attribute the difference to changes in CCN concentrations. However, this conclusion is based on gross assumptions about the macrophysical properties (including cloud optical depth) of the coastal and midocean clouds. The influence of cloud structure on broadband albedos must be studied before a more accurate assessment of the sensitivity of cloud albedo to CCN concentrations can be made.

The purpose of this study is to make qualitative assessments of the effects of both microphysics and horizontal inhomogeneity on the cloud albedo–CCN concentration relationship in a simulated marine stratus layer. The assessments are accomplished through the use of a newly developed 2D radiative transfer model and cloud field data produced by a sophisticated, 3D large eddy simulation (LES) model. The following section will describe the broadband version of the radiative transfer model used in this paper. The implementation of the broadband model is not an immediately obvious task since the addition of strong gaseous absorption greatly increases the size and computational costs of the RTM. Methods to overcome those problems are described. Section 3 presents the cloud physics data produced by the 3D LES model. Section 4 shows how the addition of CCN into the simulated cloud changed the cloud optical properties. The broadband solar albedos computed from the 2D broadband model are presented in section 5, and a comparison of the effects of microphysics and macrophysics on cloud albedo are shown in section 6. The last section summarizes the article and presents some concluding remarks.

2. Radiative transfer model

The spherical harmonic spatial grid (SHSG) method was used to provide the radiative transfer calculations for a horizontally varying medium. The SHSG method is described in detail in Evans (1993). Despite the relative computational efficiency of the SHSG method, the computer resources required for broadband calculations are large due primarily to the complications resulting from rapid variability of gas absorption coefficient with wavelength. In order to make timely broadband calculations in a two-dimensionally variable medium, a band model must be used to reduce the number of radiative transfer computations from the several thousand needed in a line by line calculation to a more reasonable number.

To account for gaseous absorption at visible and near infrared wavelengths, k-distribution data from Stackhouse and Stephens (1991) were used. The gaseous absorption data model the effects of water vapor, carbon dioxide, and oxygen for a range of wavelengths from 0.4 to 2.8 μm. For ultraviolet wavelengths from 0.28 to 0.4 μm, the ozone cross section data of Stamnes and Tsay (1990) were used. A parameterization for Rayleigh scattering (Paltridge and Platt 1976) was also included.

Following Chou (1986), the total number of gas-absorption calculations were reduced substantially by averaging the original 249-band k-distribution data over 11 bands in the solar spectrum (plus three bands using the ozone cross section data). Additionally, the number of k-value weights in the remaining bands were reduced from 37 to 9 by averaging the weights over the k domain. (See Table 1 for a description of the bandwidths used in the model.) Chou (1986) reported that reducing the number of k-values to 10 produced differences in clear-sky heating rates of less than a few percent compared to line by line calculations. For cloudy skies, however, the reduction of optical property data to 14 bands had a greater effect on the accuracy of the model. Since a cloud's optical properties vary

TABLE 1. Bandwidths used in solar broadband model.

Band	Bandwidths (μm)	Absorbing gases in band
1	3.030–3.846	H_2O
2	2.500–3.030	H_2O, CO_2
3	2.174–2.500	H_2O
4	1.887–2.174	H_2O, CO_2
5	1.667–1.887	H_2O
6	1.429–1.667	H_2O, CO_2
7	0.778–1.429	H_2O
8	0.760–0.778	H_2O, O_2
9	0.699–0.760	H_2O
10	0.692–0.699	H_2O, O_2
11	0.687–0.692	O_2
12	0.400–0.687	O_3 (cross-section data)
13	0.315–0.400	O_3 (cross-section data)
14	0.280–0.315	O_3 (cross-section data)

rapidly with respect to wavelength, the choice of wavelength used to represent each band in the radiative transfer calculations must be made judiciously.

In order to choose the representative frequency for each band, cloud-top downward solar flux and single-scattering albedo ($\tilde{\omega}$) data were computed for a marine stratocumulus layer at 249 intervals across the solar spectrum using the two-stream model described by Stackhouse and Stephens (1991). The solar flux and $\tilde{\omega}$ data were then used to compute solar flux-weighted mean single-scattering albedos for the 14-band model:

$$\tilde{\omega}_{ave} = \frac{\sum\limits_{\nu_1}^{\nu_2} \tilde{\omega}(\nu)F(\nu)}{\sum\limits_{\nu_1}^{\nu_2} F(\nu)}, \qquad (1)$$

where $\tilde{\omega}_{ave}$ is the flux-weighted mean single-scattering albedo for a particular band (14 in total), ν_1 and ν_2 are the endpoint wavelengths of that band, $F(\nu)$ are the 249-band solar flux data computed the wavelengths between ν_1 and ν_2, and $\tilde{\omega}(\nu)$ are the corresponding single-scattering albedo data. The $\tilde{\omega}$ data from the 249-band model were then used to determine those wavelengths within each band where the single-scattering albedo most closely matched the $\tilde{\omega}_{ave}$. These wavelengths were used to represent each band in Mie calculations.

In a series of two-stream model simulations, the 14-band model was compared to the original 249-band, 37 k-value weight model. The net flux convergence computed in a 1-km-thick stratocumulus with the 14-band model was within 5% of the value calculated from the 249-band model, while the differences in the albedos were less than 0.4% for a range of solar zenith angles from 10° to 75°. Since the differences in cloud albedo produced by changes in the cloud's microphysics and macrophysics in the following sections are on the order of 2%–10%, the 14-band model is expected to be adequate for the purpose of comparing albedo differences.

Since the k-distribution method requires that the radiative transfer calculations in the strongly absorbing bands involve extremely large optical depths, the computer memory requirements of the SHSG method became too large for some calculations. Fortunately, nearly all of these calculations could be neglected since most of the radiation in the stronger bands would be absorbed before reaching the top of the marine stratus layer and the weights associated with those bands were very small. In a test using a two-stream model with the same boundary conditions as the SHSG model, a flux calculation through a marine stratus cloud using all k-distribution computations was compared to a similar calculation where all of the radiative transfer computations where the SHSG model could not be used were eliminated. The differences in the flux profiles between these cases were nearly indistinguishable, and the dif-

ferences in the heating rates at any point in the cloud were less than 0.01%.

3. LES cloud fields

Multidimensional microphysical fields of sufficient density to provide optical properties to the SHSG model are not yet available from observations. In this study we utilized microphysics from simulations of a 3D marine stratus cloud field by a coupled LES–explicit microphysics version of the Regional Atmospheric Modeling System (RAMS), as described in detail by Stevens et al. (1996). Although the simulations from even the most sophisticated model are only approximations of actual cloud, one advantage of numerical models is the ability to control the external conditions in the boundary layer. A relevant example for this study is that numerical models allow for a direct investigation into the effects of CCN concentration on boundary-layer clouds independent of other effects.

Two sets of calculations were used to investigate the effects of enhanced CCN concentrations on the albedos of the marine stratus cloud. In the control run, the model simulated the marine stratus measured during the FIRE-I experiment near San Nicholas Island on 7 July 1987. The initial CCN concentration was horizontally homogeneous and matched to the measurements of Hudson and Frisbie (1991), with approximately 120 cm^{-3} nuclei activated at 1% supersaturation. The dynamical model was initialized using composite sounding data from Betts and Boers (1990). In a sensitivity test, a layer of enhanced CCN concentration (increased to six times the control run) was added above cloud top at the start of the simulations.

a. Control run

A 3D model simulation is necessary for a proper representation of the turbulent eddies in the dynamical model, but broadband radiative transfer calculations of the 3D field were found to be too computationally intensive. Instead 2D "slices" of the cloud field were used as input into the SHSG broadband model. Figure 1 shows the liquid water path (LWP) field in the control run after 9000 seconds of model simulation, which corresponds to 1800 LT 7 July. Two cross sections labeled Slice 1a and Slice 1b represent the cloud structure sampled for radiative transfer calculations presented below. These cross sections were chosen for their relative heterogeneity and to emphasize the effects of cloud geometry in the radiative transfer simulations. The mean LWP in Slices 1a and 1b were 44.8 g m^{-2} and 47.5 g m^{-2}, respectively, while the corresponding standard deviations were 24 g m^{-2} and 30 gm^{-2}.

Figure 2 presents the liquid water content (LWC) fields for Slice 1a. For computational purposes, the vertical domain in the radiative transfer calculations was limited to the region from 812.5 m (the approximate
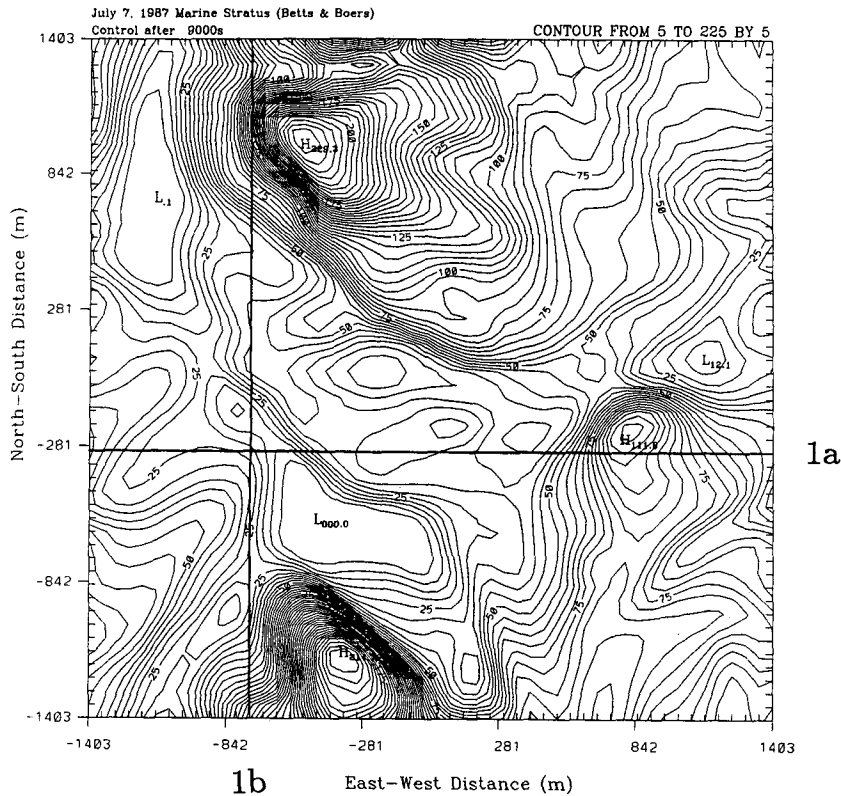
FIG. 1. The liquid water path field for the RAMS control run after 9000 seconds. The east–west cross section is labeled Slice 1a, and the north–south cross section is labeled Slice 1b.

location of the inversion) to 362.5 m above the ocean. This area contains most of the model cloud in all of the simulations. Although Fig. 2 shows horizontal variability in LWC throughout the model domain, it is important to note that the cross section would be considered to be 100% overcast from current satellite cloud
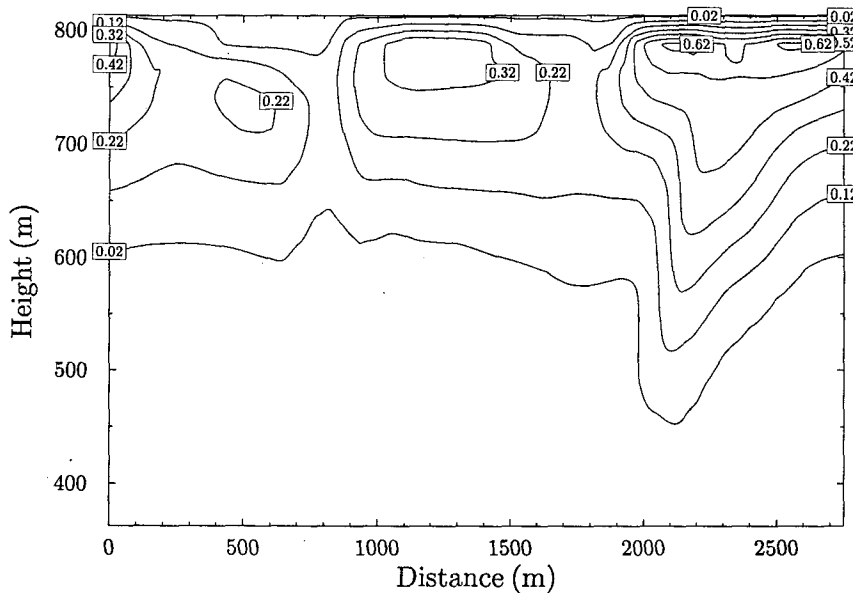

FIG. 2. The liquid water content fields (g m^{-3}) computed for cross section Slice 1a.
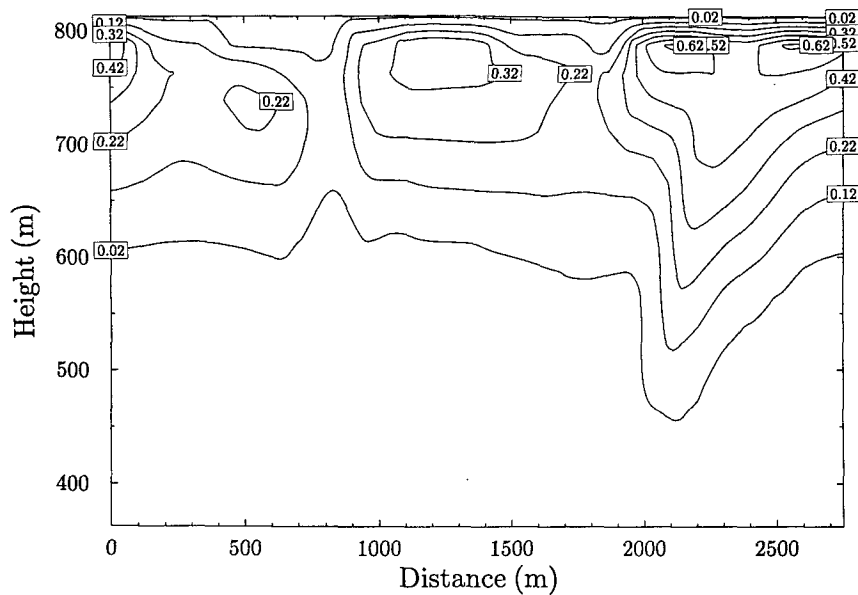
FIG. 3. As in Fig. 2 but for the sensitivity run (Slice 2a).

cover algorithms (Wielicki and Parker 1992). The effective radius generally increased with height in Slices 1a and 1b, with values near 6 μm near cloud base and 11 μm near cloud top. These values are consistent with the midcloud measurements of effective radius (between 6 and 10 μm) measured on 7 July in the FIRE I region by the University of Washington C-131A aircraft (Nakajima et al. 1991).

b. Enhanced CCN run

The sensitivity run investigated the effects of enhanced CCN concentrations that are entrained from above the cloud layer. Enhanced concentrations of aerosol above cloud top have been observed in marine stratus off the coast of California (Hegg et al. 1990) and during ASTEX (Martin et al. 1994), and this experiment examines their possible impact on the cloud layer. It is important to note that this study is a diagnostic test of the effect of enhanced CCN concentrations on the optical properties of marine stratocumulus cloud rather than an examination of the interactions between radiation and cloud dynamics. The LES model and the SHSG simulations are not coupled in any way, and any feedback between CCN changes, drizzle, and solar radiation on the cloud's physical properties is not addressed. Although the LES model contains a solar radiation parameterization that should allow the interaction between radiation and dynamics, as noted below no differences between the model dynamics of both runs (as the result of different cloud microphysical properties) developed. The sensitivity run was initialized identically to the control run, except that

above the 296-K θ level (approximately 900 m) the initial CCN concentrations were increased to six times the level in the control run. The CCN concentrations below this level were the same as in the control run.

Unlike 1D models of the atmospheric boundary layer the LES model provides entrainment rates directly. The turbulent eddies deform the upper cloud boundary and CCN are mixed in during these deformation events. When compared to observations, LES entrainment rates (near 1 cm s^{-1} in this study) are found to be reasonable (in fact, large-scale energy balances dictate that they do so). However, limitations in the observations of stratocumulus make it premature to state that LESs entrain fluid in a manner physically analogous to the natural system. Since small-scale processes (that LES models are unable to resolve) may be crucial to natural cloud-top entrainment, results dependent on the details of this process should be interpreted cautiously. Fortunately, for the experiments described here the details of how the CCN are entrained are less important than that the LES model entrains at a reasonable rate.

By the end of the simulation (9000 s), CCN concentrations were fairly well mixed throughout the boundary layer, though concentrations were larger near cloud top since the CCN were entrained from above the boundary layer. The boundary-layer mean CCN concentrations (at 1% supersaturation) in the sensitivity run were around 200 cm^{-3} by the end of the experiment.

Two cross sections at the same location as Slices 1a and 1b were taken at a model time of 9000 s (labeled as Slices 2a and 2b), and the LWC field for Slice 2a is presented in Fig. 3. Since neither the control nor the

sensitivity simulation produced significant amounts of drizzle, the CCN concentration–drizzle feedback mechanism proposed by Albrecht (1989) to increase LWP or to alter the boundary-layer thermodynamic structure was not evident in this model run. The dynamics of the boundary layer were virtually unaffected by the inclusion of the extra aerosol, and the clouds in Slices 2a and 2b look almost identical to those in Slices 1a and 1b. Although the cloud structure in both simulations look very similar, the additional aerosol in the second model run produces a cloud field with different microphysical properties. As will be shown below, these microphysical changes have a significant effect on the cloud optical properties.

4. CCN, cloud droplet, and cloud optical property relationships

Figure 4 shows how the introduction of CCN above the top of the cloud layer influences the droplet distributions in the cloud. The figure presents the domain-averaged relative difference in droplet concentration between Slice 1a and Slice 2a for several levels included in the model domain of the radiative transfer computations. The concentration of droplets smaller than roughly 11 μm in radius increased in Slice 2a (compared to Slice 1a) at almost every level in the vertical domain (362.5–812.5 m), and the magnitude of the increase was progressively larger with height. The one exception was the moderate increases at 812.5 m, which contained a mixture of

cloudy air and clear air at cloud top. Near cloud top the increase in the smallest droplet sizes was almost 200%. For most drops larger than 11-μm radius, however, the concentrations are lower in the enhanced CCN case than in the control case. The depression in larger drops is greatest in the upper levels of the cloud and demonstrates that enhanced CCN concentrations at cloud top create many more smaller droplets at the expense of larger droplets, with the greatest effects near the top of the cloud.

The increases in droplet concentrations correlate with the CCN increases in the sensitivity run, but they are a bit smaller in magnitude since the supersaturations in the cloud decreased throughout the simulation. The mean droplet concentration in Slice 2a (93.8 cm^{-3}) was almost 60% larger than the mean concentration in Slice 1a (59.5 cm^{-3}). In addition, the mean effective radius at z = 712.5 m decreased from 11.3 to 9.8 μm.

The creation of larger numbers of smaller droplets at the expense of larger droplets produced several changes in the cloud optical properties. The conversion of liquid water into greater numbers of smaller droplets increased the total cross-sectional area of the cloud particles, and thus the cloud optical depth. The optical depth changes can be most easily seen at absorbing wavelengths such as those in band 3 (2.174–2.5 μm), where the mean optical depth in Slice 1a was 6.9 but increased to 7.9 in Slice 2a. The scattering functions of smaller droplets at solar wavelengths also have a smaller forward peak, and thus the mean band 3 asymmetry factor (g) decreased from 0.828 in Slice 1a to
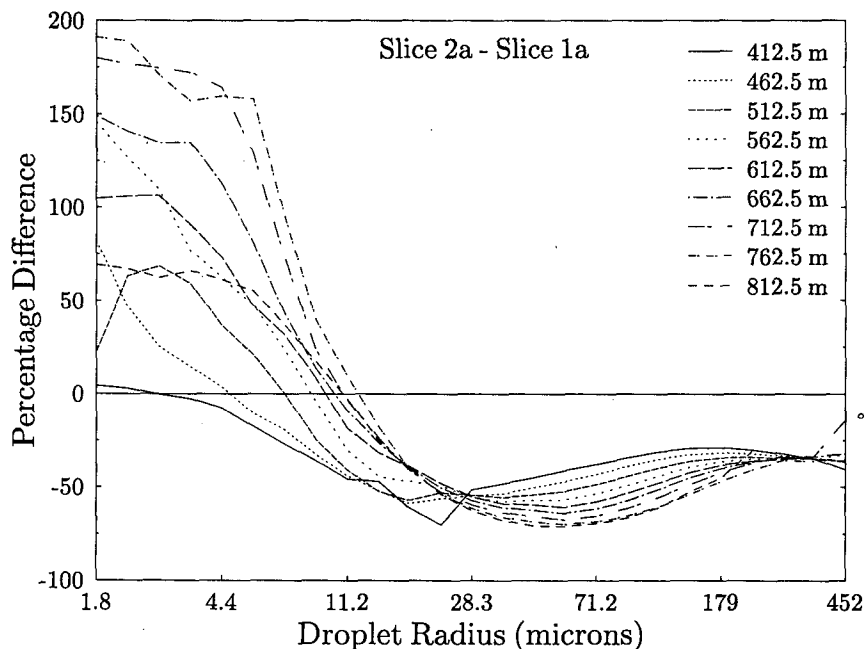

FIG. 4. The level-averaged relative differences in droplet concentration between Slices 2a and 1a as a function of the mean droplet radius in each bin of the RAMS explicit microphysics model.

0.822 in Slice 2a. Finally, for near-infrared wavelengths smaller droplet sizes produce smaller single scattering co-albedos. The single scattering co-albedo is defined as $1 - \tilde{\omega}$ and is a measure of the absorptivity of the cloud droplets. The mean single scattering co-albedos of the cloudy regions in Slices 1a and 2a were 0.0303 and 0.0264, respectively, indicating that the droplets in Slice 2a absorbed less than those in Slice 1a. The differences in optical depth, single scattering co-albedo, and asymmetry factor all worked to increase the overall cloud albedo. The next section shows how much these optical property differences changed the cloud albedo.

5. Broadband albedos

In the next two sections, three sets of radiative transfer calculations will be compared. The first set are broadband flux calculations from the SHSG model, and they represent the radiative transfer through the 2D media obtained from the RAMS simulations. These will be denoted as 2D calculations. In the second set of computations, the horizontal coupling in the SHSG model is turned off and the model atmosphere becomes a series of independent, closely spaced, horizontally homogeneous columns. This type of calculation is called the independent pixel approximation (IPA) and is used to approximate the horizontal variability of a medium with a plane-parallel model. The horizontal resolution in the IPA model was roughly 10 m to match the spacing required in the 2D model. The final form of radiative transfer calculation is the plane-parallel approximation (PPA). This method uses a single, horizontally homogeneous cloud with the domain-average optical properties of each slice to approximate the radiative transfer throughout each cross section. The domain-average properties for each level in the PPA model are simply the arithmetic means of the properties at that level in the cross section. The plane-parallel approximation has been used almost exclusively by researchers to estimate mean radiative fluxes in large-scale models.

This section will compare the broadband solar albedos derived from the three sets of calculations. The broadband solar albedo is simply defined as the ratio between the upward and downward flux at the top of the model domain (812.5 m).

a. 2D versus IPA albedos

Figure 5 shows the broadband visible (0.28–0.7 μm) albedos for Slice 1a at solar zenith angles (θ_0) of 10° and 60° for the 2D calculations and the corresponding IPA calculations. When the solar zenith angle was 10°, horizontal inhomogeneity as represented in the 2D calculations smoothed out the albedo field compared to the IPA run. When $\theta_0 = 60°$, the effects of horizontal inhomogeneity are even more noticeable. As shown in Fig. 5, a 3%–4% absolute difference between the 2D

and IPA albedos appears from 0 to 0.6 km, in the "shadow" of a large extinction maximum near the left border of the model domain. (See Fig. 2.) Near 2.0 km, the 2D albedo is 3% or 4% larger (absolute difference) than the corresponding IPA albedo and is located on the sunlit side of an extinction maxima near cloud top.

Despite the local differences in albedo, the domain-average albedo for both calculations were nearly identical. In Slice 1a for $\theta_0 = 10°$, the domain average albedos for the 2D and IPA calculations were 33.06% and 33.10%, respectively. Similar results were obtained for other completely overcast slices from both the control and sensitivity runs. For the corresponding near infrared (0.7–2.5 μm) calculations (not shown), the point by point differences between the 2D and IPA albedos were slightly larger, but like the visible albedos
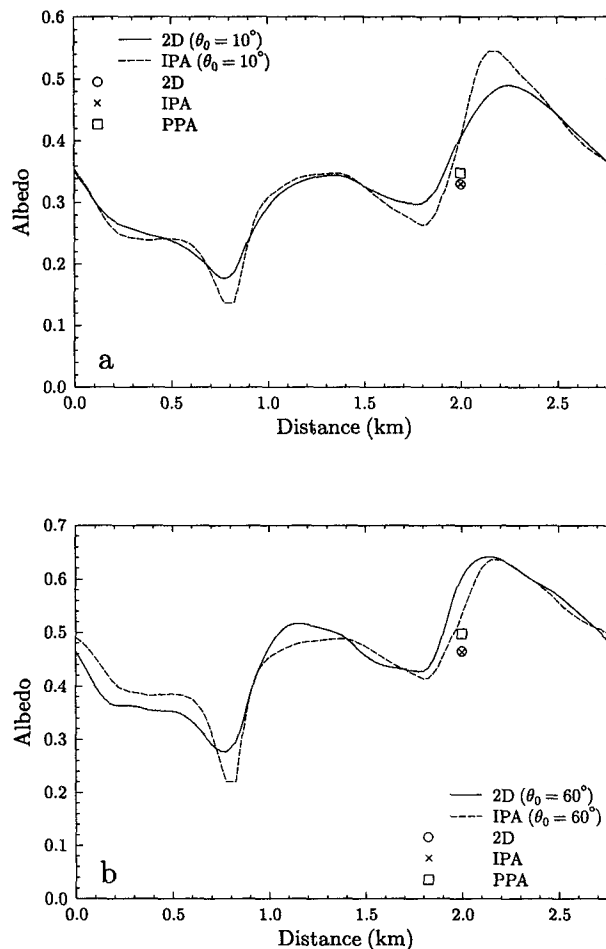

FIG. 5. The visible (0.28–0.7 μm) cloud-top albedo computed as a function of horizontal distance in Slice 1a from the 2D and IPA version of the SHSG broadband model for solar zenith angles 10° and 60°. The symbols show the domain-average cloud albedo computed from the 2D, IPA, and PPA models.

the differences in the domain-averaged 2D and IPA albedos were very small.

Figure 6 shows an example of the visible albedos computed for a cross section (Slice 3) that was not completely overcast. Slice 3 was taken from another sensitivity run not discussed in this study, but it is presented to illustrate the effects of small cloud layer breaks on 2D—IPA differences. Assuming that the minimum cloud optical depth necessary for satellite detection using the reference reflectance threshold of Wielicki and Parker (1992) (i.e., R_{clr} + 0.015) is 0.25, the cloud fraction in Slice 3 is roughly 95%. The results from the θ_0 = 60° simulation were the most striking. Slice 3 contained two small "holes" centered at 0.23 and 0.90 km along the horizontal domain. The 2D albedo in the cloudy area between the holes was significantly smaller than the IPA albedo, while the 2D albedos in the "holes" did not completely compensate this difference. This cross section showed the largest discrepancy between the 2D and IPA domain-averaged albedos, although the relative difference was still only 2%.

Small differences between multidimensional RTM and IPA cloud albeods were also found by Cahalan et al. (1994b) in a comparison between monochromatic IPA calculations and 3D Monte Carlo calculations in a simple cloud model. The results from this study extend those conclusions to broadband albedos in a more realistic cloud field and suggest that in unbroken (or nearly unbroken) marine stratus the effects of horizontal transfer of radiation on broadband solar albedos tend to cancel out over large areas. Thus, IPA calculations with spacing of the order of roughly 100 m or less are adequate for accurately computing area-averaged broadband solar albedos in marine stratus.

b. 2D/IPA versus PPA albedos

Figure 5 also shows the visible albedos in Slice 1a computed using the PPA method, as well as the domain-average values from the 2D and IPA models. The relative differences between the domain-average 2D/ IPA and PPA albedos in Slice 1a at θ_0 = 10° and θ_0 = 60° were 5.3% and 7.0%, respectively. Similar differences were computed in the other overcast cross sections. In the partly broken Slice 3, the PPA albedo was computed using a cloud-fraction-weighted average of the cloudy and clear-sky albedos derived from the cross section. The relative difference between the PPA and domain-average 2D/IPA albedos in Slice 3 was 4.6% in the θ_0 = 10° case but increased to 15% when θ_0 = 60°.

In Cahalan et al. (1994a), the positive bias in the PPA albedo compared to the IPA albedo is explained by the nonlinear relationship between cloud albedo and optical depth. The magnitude of the PPA bias in a simple fractal model of marine stratocumulus is related to a fractal parameter (f), which in turn is related to the
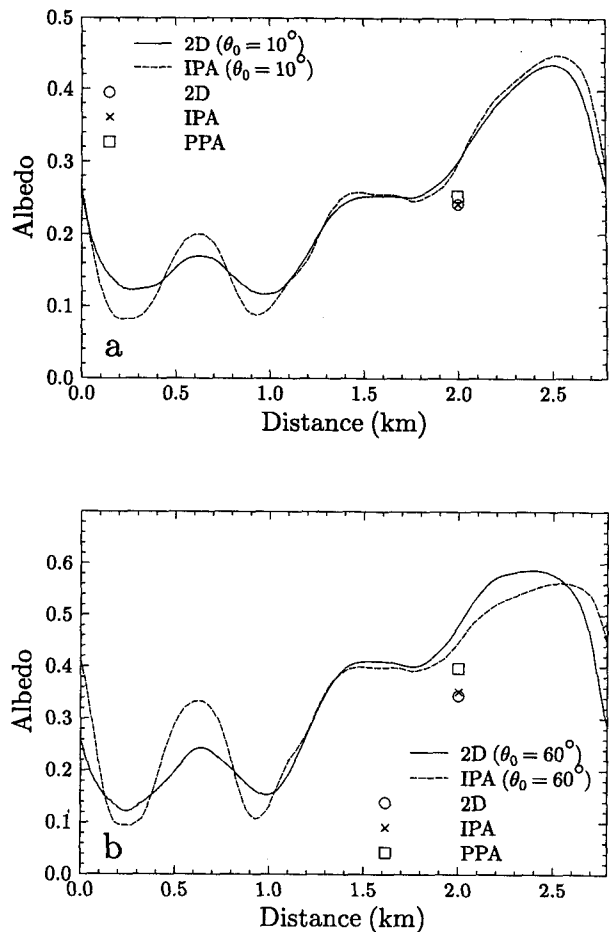

FIG. 6. The same as Fig. 5 but for Slice 3.

standard deviation of the logarithm of vertically integrated liquid water path. Since the fractal model assumes a constant effective radius, the LWP is linearly related to optical depth. In more realistic clouds like those simulated in the RAMS model, effective radius is not constant in the cloud. A better measure of the horizontal variability of the clouds used in this study would be the standard deviation of the logarithm of optical depth. In general, the use of the standard deviation of log τ rather than τ in the discussion of albedo differences is more convenient since the relationship between cloud reflectivity and log τ is approximately linear.

The standard deviation of log τ was computed at several solar wavelengths for Slices 1a, 1b, 2a, and 2b. The standard deviation values showed very little sensitivity to wavelength and ranged from 0.237 to 0.249 in band 12 (0.4–0.687 μm). These values were considerably smaller than the value presented in Cahalan et al. (1994a) as typical of the marine stratocumulus measured during the FIRE-I experiment in July 1987 (0.39) and explains why the PPA biases in this study

were smaller than those in Cahalan et al. (1994a). Estimating from Fig. 3 of Cahalan et al. (1994a), the standard deviation in log τ from the RAMS cross sections would produce relative biases for the θ_0 = 60° case in the range from 6% to 8%. This compares well with the relative biases computed for the four overcast slices (4%–8%). In Slice 3, the standard deviation of log τ was 0.468 and from the figure in Cahalan et al. (1994a) would produce an estimated PPA bias at θ_0 = 60° around 26%. The lower value of PPA bias in Slice 3 appears to be the result of the shape of the probability distribution of log τ in the cross section (Fig. 7). Unlike the other cross sections, the distribution in Slice 3 is skewed toward very low values of optical depth and does not resemble the symmetric distributions in the Cahalan et al. cloud model.

The near-infrared PPA biases were similar in magnitude to the corresponding visible PPA biases. The range in the near-infrared PPA bias in all overcast cross sections ranged from 5.4% to 6.9%, compared to the 4.3% to 7.8% range at visible wavelengths.

The relationship between optical depth and effective radius in a cloud field may have an effect on the PPA bias. The column average effective radius for each column in the IPA model was defined as

$$R_e = \frac{\sum\limits_{i=1}^{N} W_i R_{e_i}}{W_t}, \qquad (2)$$

where N is the total number of model layers in a column that have a mean liquid water content greater than 0.005 g m^{-3}, W_i is the liquid water path in layer i (g m^{-2}), R_{e_i} is the mean effective radius in layer i, and

W_t is the total liquid water path in the column. Figure 8 shows that in Slice 1a the column effective radius decreases as optical depth increases from 1 through 7 and 11 through 15, while it increases with optical depth as τ ranges from 7 to 11. The effective radius–optical depth relationship in Fig. 8 is reflected in the accompanying IPA albedo–optical depth curve. Since for a given optical depth clouds with larger droplets are less reflective than those with smaller droplets, the slight dip in the albedo–optical depth curve between optical depths from 7 to 11 is a result of the changes in effective radius with optical depth. A roughly inverse relationship between optical depth and effective radius was observed in marine stratocumulus during FIRE-I (Nakajima et al. 1991) for optically thin clouds. However, when the entire RAMS domain was sampled in this study, no correlation between optical depth and effective radius was found, and the effects of variable effective radius on the albedo–optical depth relationship of the entire cloud field are expected to be minimal.

c. Total solar albedos

The contributions from the visible and near-infrared albedos were added together to find the impacts of aerosol and horizontal inhomogeneity on the total solar broadband albedo. The domain-average total solar albedos for Slices 1a, 1b, 2a, 2b, and 3 are presented in Table 2 for the three radiative transfer models. By comparing Slice 1a to Slice 2a and Slice 1b to Slice 2b, the relative increase in total solar albedo due to the microphysical changes resulting from enhanced CCN concentrations was near 10% when the solar zenith angle was 10°, and 6% when the solar zenith angle was 60°.
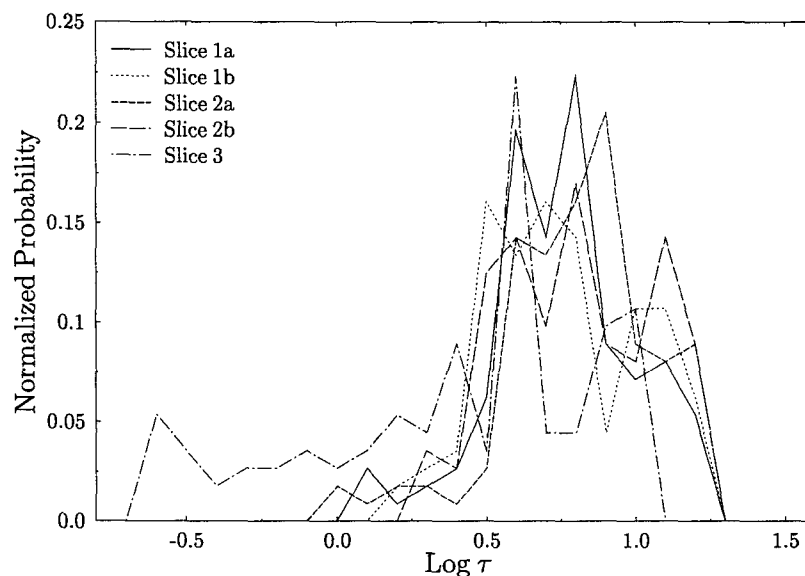

FIG. 7. The normalized probability distributions of log τ for five RAMS cross sections at band 12 (0.400–0.687 μm).
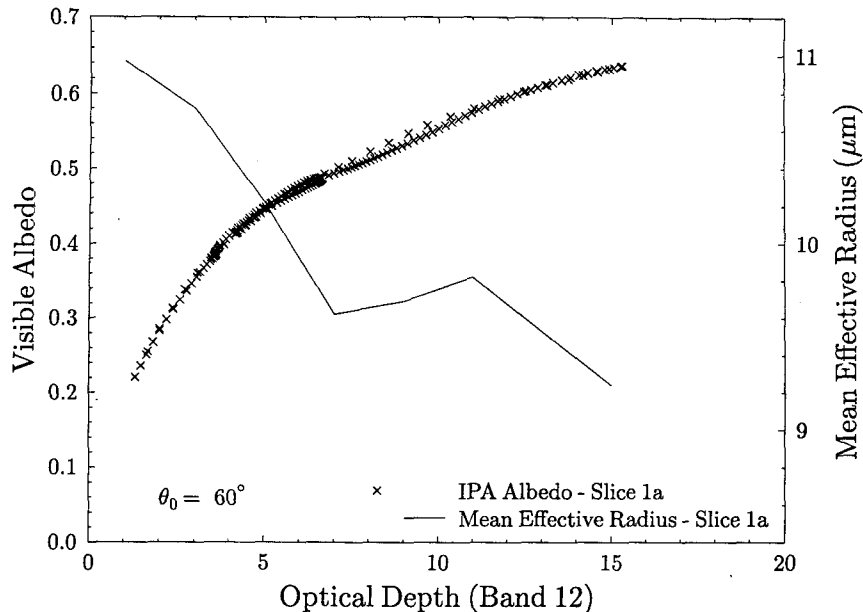
FIG. 8. The line shows the column effective radius in Slice 1a as a function of band 12 cloud optical depth. The effective radius values were binned into optical depth ranges 0.5 in width from 0 to 17. The symbols show the visible IPA albedos computed for Slice 1a at $\theta_0 = 60°$ as a function of band 12 cloud optical depth.

The PPA bias, which is a measure of the impact of horizontal inhomogeneity on albedo, was between 5% and 7% for all cross sections except for the $\theta_0 = 60°$ calculation in Slice 3 when the bias was 15%. Also, except for the low sun Slice 3 simulation, the relative differences between the 2D and IPA domain-averaged albedos were less than 1%.

6. Microphysical versus macrophysical effects

Since the domain-average albedos computed from the 2D model were approximated very well by the albedos calculated from the IPA method, an assessment of the effects of cloud microphysics and cloud structure on the 3D RAMS model domain was made by using the IPA method to compute the domain-average broadband albedo of the 3D model cloud. Gabriel and Evans (1996) have shown that at large solar zenith angles (greater than 45°) in broken clouds (with cloud fractions significantly less than 100%), the IPA-computed domain-average albedos may become inaccurate since the IPA model is not capable of accounting for the illumination of cloud sides and the effects of horizontal inhomogeneity on the "pseudosource" term of radiative transfer. However, since the 3D model domain cloud fractions in both simulations were generally near unity (usually greater than 97%), the IPA method should produce nearly the same domain average albedos as the 2D or even a 3D model would. As an added precaution to minimize possible errors, the albedos in

this section were calculated for the solar zenith angles of 10° and 40°, instead of 10° and 60°. By computing domain average albedos for each model run, this assessment allows us to examine how macrophysical variability or changes in cloud microphysics individually affect cloud albedo.

The cloud fields from the control and sensitivity runs were examined at roughly 5-min intervals from 7260- to 9000-s model time. Each cloud field (originally 52 × 52 grid points in the horizontal) was divided into four equal-size quadrants (26 × 26 grid points each) in order to increase the total number of cloud field samples and to decrease the total computational time involved in the IPA calculations. Optical depth and effective radius statistics were computed for each quadrant. By comparing the albedos of different quadrants with similar cloud optical depth and effective radius statistics, the effects of horizontal inhomogeneity and cloud microphysics on the cloud albedo may be analyzed. The optical depth for each grid point in a quadrant was computed using (3):

$$\tau = \frac{3}{2} \frac{W_t}{\rho_l R_e}, \tag{3}$$

where W_t is the gridpoint column liquid water path in grams per squared meter, ρ_l is the density of liquid water in grams per cubed centimeter, and R_e is the column effective radius in microns defined in (2) above. The optical depth and effective radius statistics com-

TABLE 2. Domain-averaged total solar (0.28–2.5 μm) albedos for the five RAMS cross sections computed from the 2D, IPA, and PPA radiative transfer models for solar zenith angles of 10° and 60°. The relative difference from the 2D model is also presented.

Slice	θ_0 (degrees) angle	RTM	Albedo	Relative difference
1a	10	2D	32.25	—%
		IPA	32.28	0.1%
		PPA	34.10	5.7%
	60	2D	47.32	—%
		IPA	47.23	−0.2%
		PPA	50.27	6.2%
1b	10	2D	32.68	—%
		IPA	32.70	0.1%
		PPA	34.41	5.3%
	60	2D	48.01	—%
		IPA	48.32	0.6%
		PPA	50.62	5.4%
2a	10	2D	35.73	—%
		IPA	35.77	0.1%
		PPA	37.79	5.8%
	60	2D	50.21	—%
		IPA	50.19	<0.1%
		PPA	53.57	6.7%
2b	10	2D	35.74	—%
		IPA	35.89	0.4%
		PPA	37.81	5.8%
	60	2D	50.89	—%
		IPA	51.31	0.8%
		PPA	53.56	5.2%
3	10	2D	23.89	—%
		IPA	23.83	−0.3%
		PPA	25.12	5.1%
	60	2D	35.59	—%
		IPA	36.36	2.2%
		PPA	40.98	15.1%

puted from selected cloud field quadrants are presented in Table 3.

a. Horizontal inhomogeneity

The effects of horizontal inhomogeneity on cloud albedo may be estimated when quadrants with similar mean statistics but different variance statistics are compared. Since the domain-average optical depth and effective radius in quadrants B1 and C1 were very similar, any differences in domain-average albedo were almost entirely due to changes in the variability (i.e., horizontal homogeneity) of the cloud fields. Quadrants A1 and D1 also had similar means but different standard deviations of optical depth and effective radius. The pairs A2/D2 and B2/C2 could also be used to examine the impact of cloud structure on cloud albedo, but the means of the optical depth and effective radius between the pairs did not match as well as those from the control run.

The domain-average albedos at $\theta_0 = 10°$ and $\theta_0 = 40°$ for the eight quadrants shown above are pre-

sented in Table 4. The domain-average albedos were computed from a 14-band, 37 k-value version of the Stackhouse and Stephens (1991) two-stream model using the Betts and Boers (1990) sounding for levels above the RAMS model domain.

The relative differences in the domain-averaged albedos between quadrants A1/D1 and quadrants B1/C1 at $\theta_0 = 10°$ were 4.8% and 3.0%, respectively. Similar differences were found for a solar zenith angle of 40°. As expected, the quadrants with the larger standard deviation in log τ (producing the larger PPA bias) had the lower albedo. The larger albedo differences between quadrants A1 and D1 reflect the larger differences in the variance of the optical property distribution. The relative differences in the albedos between quadrants A2/D2 and quadrants B2/C2 at $\theta_0 = 10°$ were 2.9% and 2.2%, respectively. The differences in the sensitivity run were smaller than in the control run since the larger differences in mean optical depth in each pair partially counteracted the macrophysical effects.

A comparison of the standard deviation of log τ and R_e between the control run quadrants and the sensitivity run quadrants showed only small increases in the variance of the cloud optical properties. For example, at 9000 s in the control run the standard deviation of log τ for the entire domain was 0.450 and the standard deviation of R_e was 0.764 μm. In the sensitivity run at 9000 s the corresponding standard deviations were 0.482 and 0.807 μm. Compared to the 0.243 increase in the standard deviation of log τ from quadrants A1 to D1 and a similar 0.187 difference between quadrants B1 and C1, the overall difference in the standard deviation of log τ between the control and sensitivity runs (0.032) is small. This result suggests that the effects of aerosol on cloud albedo in this study are mostly due to changes in microphysics rather than changes in cloud inhomogeneity.

b. Microphysics

The effect of cloud microphysical changes on cloud albedo may be computed from the quadrant pairs A1/A2, B1/B2, C1/C2, and D1/D2, which have similar cloud geometries and similar variance statistics (especially the A1/A2 and B1/B2 pairs) but different mean properties as the result of the enhanced CCN concentrations in the sensitivity run.

The relative differences in the domain average albedo (for $\theta_0 = 10°$) between the corresponding quadrants from the control run and the sensitivity run (A1/A2, B1/B2, C1/C2, and D1/D2) were 6.9%, 5.7%, 6.5%, and 9.1%, respectively. The larger differences between quadrants D1 and D2 were the result of the larger microphysical changes between the control run and the sensitivity run at the end of the model run compared to earlier times.

TABLE 3. Optical depth and effective radius statistics computed for selected cloud field quadrants from the RAMS model runs. The quadrants are identified by the model run, model time, and quadrant number. The effective radius statistics are in units of microns.

Quadrant name	Model run	Model time	Quadrant location	$\bar{\tau}$	$\bar{R}_e$	Standard deviation (log τ)	Standard deviation (R_e)
A1	control	7560 s	top right	6.87	10.33	0.335	0.668
B1	control	7560 s	bottom right	7.97	10.70	0.313	0.674
C1	control	8460 s	bottom right	7.99	10.60	0.500	0.591
D1	control	9000 s	bottom left	6.96	10.34	0.578	0.855
A2	sens. 1	7560 s	top right	7.50	9.51	0.347	0.666
B2	sens. 1	7560 s	bottom right	8.49	9.95	0.316	0.674
C2	sens. 1	8460 s	bottom right	8.75	9.60	0.547	0.768
D2	sens. 1	9000 s	bottom left	7.80	9.10	0.631	0.899

7. Summary and concluding remarks

This article investigated the relative impacts of enhanced cloud condensation nuclei (CCN) and horizontal inhomogeneity on the broadband albedo of a 3D cloud field simulated by an LES model. The Regional Atmospheric Modeling System (RAMS) simulated a marine stratus cloud deck based on measurements from the 7 July 1987 FIRE-I experiment near San Nicholas Island. In a second model run, the sensitivity of cloud optical properties to enhanced CCN concentrations was tested by initializing RAMS with six times the observed CCN above cloud top. As expected, the enhanced CCN concentrations at cloud top created greater numbers of smaller droplets in the cloud compared to the control run and changed the optical properties of the cloud to make it more reflective. For example, in the near infrared from 2.17 to 2.5 μm, the optical depth in the sensitivity run was 14% larger than the control run, while the single scattering coalbedo decreased 13% and the asymmetry factor decreased slightly.

Optical properties derived from 2D cross sections of the RAMS simulations were used as input for a 2D broadband model, and the results of three types of radiative transfer calculation were presented. The 2D calculations simulating the radiative transfer through the 2D cross sections were compared to independent pixel

TABLE 4. Domain-averaged solar albedos computed from IPA calculations of selected cloud field quadrants from the RAMS model runs. The 14-band, 37 k-value version of Stackhouse and Stephens (1991) was used to compute the broadband fluxes from 0.28 to 2.8 nm at solar zenith angles of 10° and 40°.

Quadrant name	Albedo ($\theta_0 = 10°$)	Albedo ($\theta_0 = 40°$)
A1	38.59	40.62
B1	41.59	43.58
C1	40.34	42.21
D1	36.75	38.73
A2	41.27	43.30
B2	43.96	45.95
C2	42.98	44.82
D2	40.08	42.03

approximation (IPA) calculations that neglect the horizontal transport of radiation between adjacent columns in the model and to plane-parallel (PPA) calculations that use domain-average cloud optical properties of the cross section to estimate mean cloud radiative properties. A comparison of the point by point 2D and IPA albedos showed significant local differences in the broadband solar albedo but nearly identical domain averages and indicated that the overall effects of the horizontal transport of broadband solar radiation on domain-averaged albedo were negligible in unbroken stratus. The albedos calculated in a partly broken cross section suggest that small breaks in cloud cover may result in small differences between multidimensional and IPA domain-average albedos at large solar zenith angles.

Calculations of the PPA broadband albedo bias relative to the IPA albedo were generally consistent with the monochromatic results of Cahalan et al. (1994a) and extend the conclusions from that study to broadband albedos in a more realistic cloud model. The impact of cloud structure on the mean broadband solar albedo in unbroken (or nearly unbroken) marine stratus therefore came mainly from the horizontal variability of optical depth and the nonlinear relationship between albedo and optical depth rather than effects due to the horizontal transport of solar radiation. Variations in the mean effective radius of the cloud field were found to have only a small influence on the albedo–optical depth relationships and the overall PPA bias of the simulated cloud.

Given the good agreement between the domain-averaged albedos computed by the IPA and 2D methods in this study and similar results from Cahalan et al. (1994b), computations of the mean albedo over portions of the 3D RAMS domain were made for both RAMS simulations using IPA calculations from a two-stream model. The relative differences in cloud albedo due to microphysical changes resulting from the sixfold increase of CCN concentration above cloud top ranged from 6% to 9%. (In the estimation of the sensitivity of albedo to a given change in CCN concentration it is important to remember that the mean CCN concentrations below the inversion

layer in the sensitivity run increased only 67%. The efficiency at which the boundary layer can scavenge enhanced aerosol concentrations depends on many factors, including the entrainment rate and the original location of the aerosol within the boundary layer.) A comparison between the domain-average solar albedos computed for cloud fields that have optical properties with similar means but different variances showed that the relative difference in cloud albedo resulting from the differences in the variance of cloud optical properties were between 3% and 5%.

The CCN concentration sensitivity test suggests that locally the effects of internal inhomogeneity on broadband albedo when compared to a horizontally homogeneous cloud with the same mean optical properties (i.e., the PPA bias) can be nearly as large as the microphysically induced changes produced by the entrainment of increased CCN concentrations from above the cloud layer. Differences in the horizontal inhomogeneity between the control run and the aerosol sensitivity run were small in this study since the dynamics in both runs were virtually identical and contributed very little to the overall differences in cloud albedo. In the LES simulations, however, there was little solar radiation interaction and almost no drizzle formation that could have altered the dynamics between the runs. More research into the interactions between CCN concentration, solar radiation, drizzle, and cloud dynamics and its possible effects on the horizontal inhomogeneity of marine stratus is needed. A follow-up paper examining the interactions between enhanced CCN concentration and drizzle and their effects on cloud structure is under way.

REFERENCES

Albrecht, B. A., 1989: Aerosols, cloud microphysics, and fractional cloudiness. *Science,* **245,** 1227–1230.

Betts, A. K., and R. Boers, 1990: A cloudiness transition in a marine boundary layer. *J. Atmos. Sci.,* **47,** 1480–1497.

Boucher, O., and H. Rodhe, 1994: The sulfate–CCN–cloud albedo effect—A sensitivity study with 2 general-circulation models. *Tellus,* **47B,** 281–300.

Cahalan, R. F., W. Ridgway, W. J. Wiscombe, T. L. Bell, and J. B. Snider, 1994a: The albedo of fractal stratocumulus clouds. *J. Atmos. Sci.,* **51,** 2434–2455.

——, ——, ——, S. Gollmer, and Harshvardhan, 1994b: Independent pixel and Monte Carlo estimates of stratocumulus albedo. *J. Atmos. Sci.,* **51,** 3776–3790.

Charlson, R. J., J. E. Lovelock, M. O. Andreae, and S. G. Warren, 1987: Oceanic phytoplankton, atmospheric sulphur, cloud albedo and climate. *Nature,* **326,** 655–661.

Chou, M. D., 1986: Atmospheric solar heating rate in the water vapor bands. *J. Climate Appl. Meteor.,* **25,** 1532–1542.

Coakley, J. A., Jr., R. L. Bernstein, and P. A. Durkee, 1987: Ship tracks etc. *Science,* **237,** 1020.

Evans, K. F., 1993: Two-dimensional radiative transfer in cloudy atmospheres: The spherical harmonic spatial grid method. *J. Atmos. Sci.,* **50,** 3111–3124.

Gabriel, P. M., and K. F. Evans, 1996: Simple radiative transfer methods for calculating domain-averaged solar fluxes in inhomogeneous clouds. *J. Atmos. Sci.,* **53,** 858–877.

Hegg, D. A., L. F. Radke, and P. V. Hobbs, 1990: Particle production associated with marine clouds. *J. Geophys. Res.,* **95,** 13 917–13 926.

Hudson, J. G., and P. R. Frisbie, 1991: Cloud condensation nuclei near marine stratus. *J. Geophys. Res.,* **96,** 20 795–20 808.

Jones, A., D. L. Roberts, and A. Slingo, 1994: A climate model study of indirect radiative forcing by anthropogenic sulphate aerosols. *Nature,* **370,** 450–453.

Kim, Y., and R. D. Cess, 1993: Effect of anthropogenic sulfate aerosols on low-level cloud albedo over oceans. *J. Geophys. Res.,* **98,** 14 883–14 885.

Martin, G. M., D. W. Johnson, and A. Spice, 1994: The measurement and parameterization of effective radius of droplets in warm stratocumulus clouds. *J. Atmos. Sci.,* **51,** 1823–1842.

Nakajima, T., M. D. King, J. D. Spinhirne, and L. F. Radke, 1991: Determination of the optical thickness and effective particle radius of clouds from reflected solar radiation measurements. Part II: Marine stratocumulus observations. *J. Atmos. Sci.,* **48,** 728–750.

Paltridge, G. W., and C. M. R. Platt, 1976: *Radiative Processes in Meteorology and Climatology.* Elsevier, 318 pp.

Slingo, A., 1990: Sensitivity of the earth's radiation budget to changes in low clouds. *Nature,* **343,** 49–51.

Smith, G. L., J. T. Suttles, and N. Manalo, 1989: The erbe alongtrack scan experiment. *IRS '88: Current Problems in Atmospheric Radiation,* J. Lenoble and J. F. Geleyn, Eds., A. Deepak, 242–244.

Stackhouse, P. W., Jr., and G. L. Stephens, 1991: A theoretical and observational study of the radiative properties of cirrus: Results from FIRE 1986. *J. Atmos. Sci.,* **48,** 2044–2059.

Stamnes, K., and S. C. Tsay, 1990: Optimum spectral resolution for computing atmospheric heating and photodissociation rates. *Planet. Space Sci.,* **38,** 807–820.

Stevens, B., G. Feingold, W. R. Cotton, and R. L. Walko, 1996: Elements of the microphysical structure of numerically simulated nonprecipitating stratocumulus. *J. Atmos. Sci.,* **53,** 980–1006.

Stuhlmann, R., P. Minnis, and G. L. Smith, 1985: Cloud bidirectional reflectance functions: A comparison of experimental and theoretical results. *Appl. Opt.,* **24,** 396–401.

Twomey, S., 1977: The influence of pollution on the short wave albedo of clouds. *J. Atmos. Sci.,* **34,** 1149–1152.

Wielicki, B. A., and L. Parker, 1992: On the determination of cloud cover from satellite sensors: The effect of sensor spatial resolution. *J. Geophys. Res.,* **97,** 12 799–12 823.